

Article

N-Doped CrS₂ Monolayer as a Highly-Efficient Catalyst for Oxygen Reduction Reaction: A Computational Study

Zengming Qin ¹, Zhongxu Wang ¹, Xiaofeng Li ², Qinghai Cai ², Fengyu Li ^{3,*} and Jingxiang Zhao ^{1,2,*}

¹ Key Laboratory for Photonic and Electronic Bandgap Materials, Ministry of Education, School of Physics and Electronic Engineering, Harbin Normal University, No. 1, Shida Street, Harbin 150025, China

² College of Chemistry and Chemical Engineering, Harbin Normal University, Harbin 150025, China

³ School of Physical Science and Technology, Inner Mongolia University, Hohhot 010021, China

* Correspondence: fengyuli@imu.edu.cn (F.L.); zhaojingxiang@hrbnu.edu.cn (J.Z.)

Abstract: Searching for low-cost and highly-efficient oxygen reduction reaction (ORR) catalysts is crucial to the large-scale application of fuel cells. Herein, by means of density functional theory (DFT) computations, we proposed a new class of ORR catalysts by doping the CrS₂ monolayer with non-metal atoms (X@CrS₂, X = B, C, N, O, Si, P, Cl, As, Se, and Br). Our results revealed that most of the X@CrS₂ candidates exhibit negative formation energy and large binding energy, thus ensuring their high stability and offering great promise for experimental synthesis. Moreover, based on the computed free energy profiles, we predicted that N@CrS₂ exhibits the best ORR catalytic activity among all considered candidates due to its lowest overpotential (0.41 V), which is even lower than that of the state-of-the-art Pt catalyst (0.45 V). Remarkably, the excellent catalytic performance of N@CrS₂ for ORR can be ascribed to its optimal binding strength with the oxygenated intermediates, according to the computed linear scaling relationships and volcano plot, which can be well verified by the analysis of the p-band center as well as the charge transfer between oxygenated species and catalysts. Therefore, by carefully modulating the incorporated non-metal dopants, the CrS₂ monolayer can be utilized as a promising ORR catalyst, which may offer a new strategy to further develop eligible electrocatalysts in fuel cells.

Keywords: CrS₂ monolayer; non-metal doping; oxygen reduction reaction; overpotential; density functional theory



Citation: Qin, Z.; Wang, Z.; Li, X.; Cai, Q.; Li, F.; Zhao, J. N-Doped CrS₂ Monolayer as a Highly-Efficient Catalyst for Oxygen Reduction Reaction: A Computational Study. *Nanomaterials* **2022**, *12*, 3012. <https://doi.org/10.3390/nano12173012>

Academic Editor: Frederik Tielens

Received: 18 July 2022

Accepted: 29 August 2022

Published: 30 August 2022

Publisher's Note: MDPI stays neutral with regard to jurisdictional claims in published maps and institutional affiliations.



Copyright: © 2022 by the authors. Licensee MDPI, Basel, Switzerland. This article is an open access article distributed under the terms and conditions of the Creative Commons Attribution (CC BY) license (<https://creativecommons.org/licenses/by/4.0/>).

1. Introduction

The rising energy demand and depletion of fossil fuels have attracted increasing interest in alternative energy sources. This is because the traditional fossil fuels are not renewable and will produce harmful combustion products, such as CO, CO₂, NO, and SO₂, which thus pose a serious challenge to human health and environmental protection [1–6]. In this regard, electrochemical energy storage and conversion technologies, such as fuel cells, were regarded as efficient and clean devices for reducing the global energy shortage [7,8]. However, the efficiency of these energy-related devices was greatly determined by the oxygen reduction reaction (ORR) due to its sluggish kinetics and high overpotential [9–13]. At present, Pt-based materials represent the most promising ORR catalysts [14–17]. However, their practical application is severely limited by their high price and low abundance. Thus, the search for highly efficient, low-cost alternative electrocatalysts is urgent to boost the ORR.

In recent years, single-layer transition metal dichalcogenides (TMDs) have become a hotspot of theoretical and experimental research owing to their large surface area, stability, and peculiar electronic structure [18–23]. Thus, TMD-based materials have been widely employed in nanoelectronics, nanophotonics, the absorber layer in solar cells, anode materials, field-effect transistors, and so on [24–28]. More interestingly, the heteroatom doped TMDs

have attracted great interest because they have more active sites, low cost, high stability, and high efficiency as potential electrocatalytic catalysts [29–35]. For example, Xiong et al. reported that co-doped MoS₂ possesses high catalytic activity for oxygen evolution reaction [29]. Moreover, Lv et al. proposed that N-doped MoS₂ displayed a high faradaic efficiency and low onset overpotential for CO₂ electroreduction to CO [30]. Theoretically, Li et al. demonstrated that B-doping causes the VS₂ monolayer to exhibit outstanding catalytic activity towards nitrogen reduction reactions [31]. Moreover, Singh et al. reported that the ORR activity of N-doped WS₂ monolayers should originate from the introduction of spin density caused by N doping [32]. In addition, Tian et al. showed that Co doped 1T-TiS₂ exhibits significantly enhanced performance toward the ORR [33].

As a representative of 2D TMDs, the chromium disulfide (CrS₂) monolayer was synthesized via the chemical vapor deposition (CVD) method in 2019 [21]. Interestingly, due to its unique properties, the CrS₂ monolayer has wide applications in spintronic devices [36,37]. For example, Chen et al. suggested that CrS₂ has the most diverse electronic and magnetic properties: antiferromagnetic (AFM) metallic, non-magnetic (NM) semiconductor, and ferromagnetic (FM) semiconductor with a Curie temperature of ~1000 K [36]. Moreover, Zhang et al. reported that the magnetic properties of CrC₂ monolayer can be effectively tuned by doping metal atoms [37].

Inspired by the interesting properties of the CrS₂ monolayer, in this work, we explored the potential of several non-metal-doped CrS₂ monolayers (X@CrS₂, X = B, C, N, O, Si, P, Cl, As, Se, and Br) as ORR catalysts by performing comprehensive DFT computations. According to the computed formation energies and binding energies of these X@CrS₂ systems, we suggested that these doped CrS₂ candidates are very likely to be synthesized in experiments and possess extremely high stability. Moreover, the N@CrS₂ catalyst was screened out as an eligible ORR catalyst with a rather low overpotential of 0.41 V, which originates from its optimal binding strengths with oxygenated intermediates based on the linear scaling relationships and volcano plot.

2. Materials and Methods

All computations were performed based on spin-polarized density functional theory, as implemented in the Vienna ab initio simulation package (VASP 5.4.1) [38,39]. The projector augmented wave (PAW) was adopted to describe the interactions between ions and electrons [40,41]. The generalized gradient approximation (GGA) in the form of Perdew–Burke–Ernzerhof (PBE) was adopted for the exchange–correlation functional [42]. Notably, the PBE functional is, nowadays, the most commonly used functional for solid-state calculations, which remains the best for the solids containing 3d-transition elements [43–45]. In particular, our purpose in the present work is to search for the ideal ORR catalysts among various candidates, and we thus mainly focus on the catalytic tendency of these candidates for ORR. Thus, although some more modern and better functionals have been proposed in recent years [46,47], the identified scaling relations of oxygenated species on various electrocatalysts and the derived conclusions (such as the corresponding catalytic activity) will not change. The DFT+D3 method in the Grimme scheme was employed to describe the possible weak interactions of the oxygenated species and the catalysts [48]. An energy cutoff of 500 eV was used for the plane wave (Table S1), and the convergence criteria of force and energy were set to 0.02 eV Å^{−1} and 10^{−5} eV, respectively. A k-point of 3 × 3 × 1 was sampled in the Brillouin zones (Table S1), and the vacuum space was set to 15 Å.

To estimate the ORR catalytic performance of these X@CrS₂ materials, the change in the Gibbs free-energy change (ΔG) of each elementary reaction step during ORR was computed using the computational hydrogen electrode (CHE) model [15,49]: $\Delta G = \Delta E + \Delta ZPE - T\Delta S + \Delta G_U$, in which ΔE is the reaction energy directly obtained from DFT computations, and ΔZPE and ΔS represent the difference of zero-point energy and entropy, respectively, which can be derived from the computations on the vibrational frequencies and the standard thermodynamic data. $\Delta G_U = -eU$, where U is the applied potential. Since DFT generally fails to obtain the energy of the O₂ molecule, the free energy of O₂ (G_{O_2})

will be computed via the energies of H_2O and H_2 , namely $G_{\text{O}_2} = G_{\text{H}_2\text{O}} - 2G_{\text{H}_2} + 4.92 \text{ eV}$. Furthermore, the ORR's catalytic activity was evaluated by computing the corresponding overpotential (η) according to the following equations: $\eta = \max\{\Delta G_1, \Delta G_2, \Delta G_3, \Delta G_4\}/e + U^0$, where ΔG represents the free energy change in each elementary reaction, including the formation of OOH^* , O^* , and OH^* and the desorption of OH^* , and U^0 is the equilibrium potential of ORR, which is equal to 1.23 V. According to the above definition, a smaller η value corresponds to a higher catalytic activity for ORR.

3. Results

3.1. Structures, Stabilities, and Properties of $X\text{@CrS}_2$ Catalysts

First, we investigated the structures and electronic properties of the pristine CrS_2 monolayer with the 2H phase. As shown in Figure 1a, each Cr center is prismatic coordinated by six surrounding S atoms, with the S atoms in the upper layer lying directly above those of the lower layer. Furthermore, the optimized lattice constant for the CrS_2 monolayer is 3.04 Å, while the lengths of the formed Cr-S bonds are 2.28 Å. Moreover, the CrS_2 monolayer is a direct semiconductor with the band gap of 0.93 eV, in which the conduction band minimum and the valence band maximum located at the K point mainly originate from the contribution of 3d orbitals of the Cr atom (Figure 1b). Notably, these above results on the structure and properties of a pristine CrS_2 monolayer are consistent with previous theoretical reports [50], indicating the accuracy of our computational methods to describe the behavior of the CrS_2 monolayer.

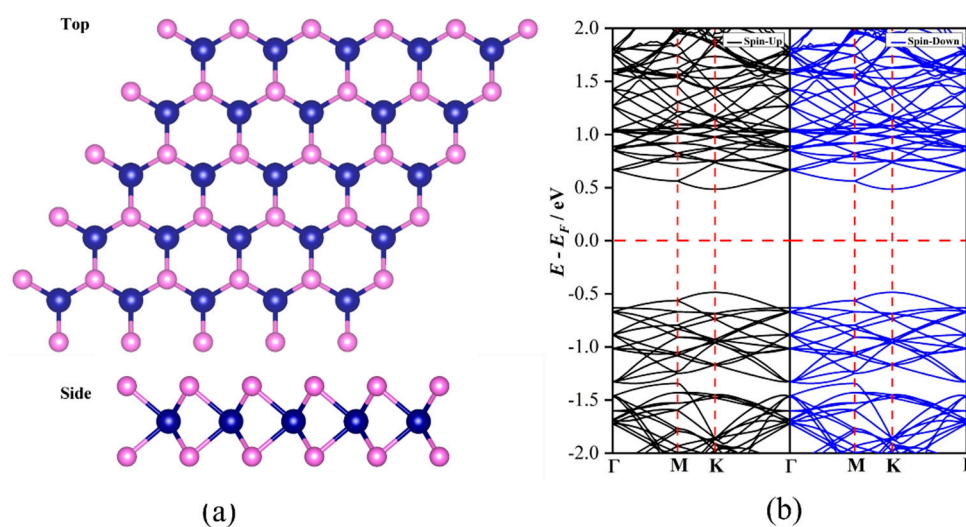


Figure 1. (a) The obtained stable configurations and (b) computed band structure for the pristine CrS_2 monolayer.

Based on the optimized CrS_2 monolayer, various non-metal atoms were introduced to substitute one of the S atoms within the CrS_2 monolayer to construct the doped CrS_2 system. After fully geometrical relaxation, the structures of the $X\text{@CrS}_2$ monolayer are presented in Figure 2, while their corresponding structural parameters are summarized in Table 1. The results showed that, after the introduction of dopants, the structure of the CrS_2 monolayer is changed in various ways, which are highly dependent on the difference in the radius between dopants and S atoms. In detail, for B, C, N, and O dopants with a smaller radius than the S atom, the introduced non-S atoms are *concave* from the CrS_2 plane, whereas the doping of Si, P, Cl, As, Se, and Br induces an unchanged or slightly outward structure due to their comparable or slightly larger radius.

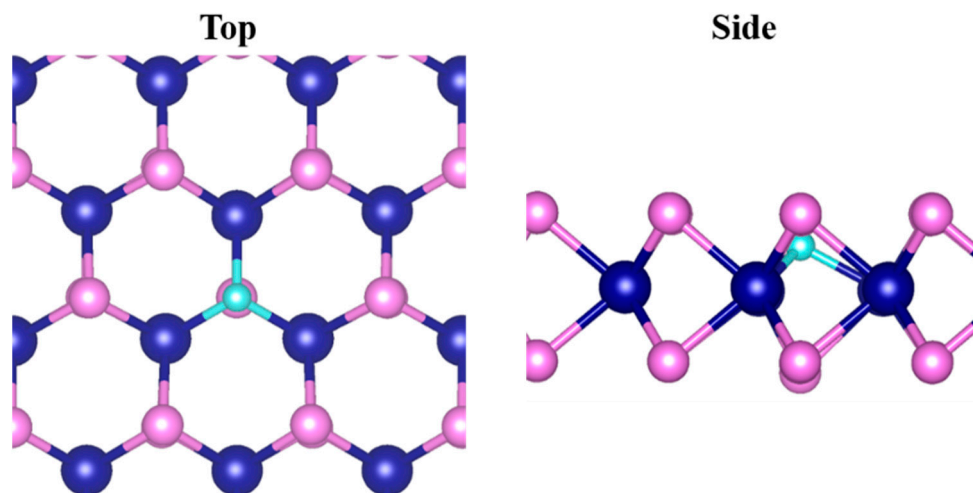


Figure 2. The obtained stable configurations for $X@CrS_2$ monolayers (N@CrS₂ was chosen as a representative).

Table 1. The computed bond's length of X-Cr (d_{X-Cr} , Å), formation energies (E_f , eV), binding energies (E_{bind} , eV), magnetic moment (μ_B), charge transfer (Q, e⁻), and band gaps (E_{gap} , eV) for various $X@CrS_2$ monolayers.

	d_{X-Cr}	E_f		E_{bind}	μ_B	Q	E_{gap}
		S-rich	Cr-rich				
pristine	2.28	/	/	/	0.00	/	0.93
B	1.97	2.06	0.94	-5.62	1.00	0.09	0.20
C	1.92	0.76	-0.36	-7.16	0.01	0.77	0.90
N	1.87	0.16	-0.96	-5.75	1.00	0.94	0.25
O	1.93	-2.70	-3.83	-6.96	0.01	0.95	0.96
Si	2.47	-3.40	-4.53	-3.93	2.00	0.32	0.27
P	2.35	0.15	-0.97	-4.15	1.00	0.27	0.95
Cl	2.41	-2.48	-3.61	-3.14	1.00	0.47	0.18
As	2.49	-0.02	-1.14	-3.70	0.96	0.04	0.00
Se	2.42	-1.17	-2.30	-4.76	0.01	0.28	0.98
Br	2.56	-0.46	-1.58	-2.52	1.00	0.31	0.19

To assess the experimental feasibility of these doped CrS₂ monolayers, we computed their formation energies (E_f) based on the following equation: $E_f = E_{X@CrS_2} - E_{CrS_2} + \mu_S - \mu_X$ [51,52], where the $E_{X@CrS_2}$ and E_{CrS_2} are the total energies of doped and pristine CrS₂ monolayers, respectively. μ_X and μ_S are the chemical potentials of a doping atom and S atom. Notably, μ_X can be derived from the energy per atom in their bulk X materials. In contrast, μ_S is dependent on the growth conditions, in which two extreme cases were considered, including Cr-rich and S-rich conditions. According to previous studies [32,53], the μ_{Cr} and μ_S should meet the relationship from the thermodynamic equilibrium condition: $\mu_{CrS_2} = \mu_{Cr} + 2\mu_S$, where μ_{CrS_2} represents the total energy of the pristine CrS₂ monolayer per formula unit. Under Cr-rich conditions, the μ_{Cr} was taken from the bulk Cr. Thus, μ_S can be obtained by: $\mu_S = (\mu_{CrS_2} - \mu_{Cr})/2$. On the other hand, under S-rich conditions, the μ_S can be obtained from its bulk S₈ state, and then μ_{Cr} can be determined by: $\mu_{Cr} = \mu_{CrS_2} - 2\mu_S$. The computed formation energies of these $X@CrS_2$ materials were listed in Table 1. We can see that the formation energies for B doping are all positive values, indicating that the formation of this kind of doped CrS₂ monolayer is difficult. On the contrary, when O, Si, Cl, As, Se, and Br dopants were introduced into the CrS₂ monolayer, their E_f values were always negative, implying notable feasibility for their experimental synthesis. Notably, the CrS₂ monolayers doped by C, N, and P atoms are more likely to form under Cr-rich conditions due to their negative formation energies. Obviously, by carefully tuning the

reaction conditions, these doped CrS₂ monolayers can be easily fabricated in experiments, except for B-doping.

To further explore the structural stability of X@CrS₂, we computed the binding energies (E_{bind}) of the introduced dopants on the CrS₂ monolayer according to the following equation: $E_{bind} = E_{X@CrS_2} - E_{CrS_2} - E_X$, where $E_{X@CrS_2}$, E_{CrS_2} , and E_X represent the total electronic energies of doped CrS₂ monolayers, the defective CrS₂ substrate, and isolated X atoms in their most stable phase. It can be observed that the E_{bind} values of these dopants on the CrS₂ substrate range from -2.52 eV of Br to -7.16 eV of C, indicative of the strong binding strength, thus ensuring their high stability. The stability of X@CrS₂ was further evaluated by using AIMD simulations, where N doping was taken as a representative. As shown from Figure S1, there is still no significant distortion of the geometric structure at 500 K, indicative of its high thermodynamic stability. It should be noted that incorporation of various non-metal atoms into 2D TMDs has been already realized experimentally. For example, Li et al. reported a simple, facile, and effective strategy to fabricate an N-doped MoS₂ nanosheet [54], while Xin et al. demonstrated the fabrication of a P-doped MoS₂ nanosheet by the one-step hydrothermal method [55]. Therefore, we strongly believe that the as-designed doped CrS₂ monolayer holds great promise for synthesis.

Next, we explored the magnetic and electronic properties of these X@CrS₂ systems. Our results showed that the pristine CrS₂ monolayer is a nonmagnetic material. After introducing these dopants into the CrS₂ monolayer, however, different magnetic behaviors can be observed: (1) C-, O-, and Se-doped CrS₂ systems still retain their nonmagnetic states due to the absence of unpaired electrons; (2) as for B, N, P, As, or Br-doped systems, the total magnetic moment is close to $1.00 \mu_B$, while the Si-doped CrS₂ monolayer has a magnetic moment of $2.00 \mu_B$. Moreover, we noted that these dopants will loot different amounts of electrons ($0.04\sim 0.95 |e^-|$) from the CrS₂ monolayer, except for the Si dopant, which can donate about 0.32 electrons to the CrS₂ substrate. As a result, the band gaps of the doped CrS₂ monolayer are reduced to different degrees due to the introduction of impurity levels. For example, the N-doped CrS₂ system exhibits a smaller band gap of 0.25 eV than that of the pristine one (0.99 eV), suggesting the enhanced electrical conductivity, which may facilitate the rapid charge transfer in electrocatalysis [56]. It is noted that the GGA method usually underestimates band gaps, whereas the hybrid functional method, such as Heyd–Scuseria–Ernzerhof (HSE06), can rectify the band gap [57]. For example, the computed band gaps of the well-established MoS₂ monolayer using HSE06 and PBE methods are 2.20 and 1.79 eV [58], respectively. Despite the fact that a more accurate band gap value can be predicted by means of the HSE06 method, the corresponding computational cost is extremely high for the 10 doped CrS₂ monolayers, which consist of 25 Cr and 50 S atoms. We will mainly focus on the trend of the band gaps of the CrS₂ monolayer after non-metal doping.

3.2. ORR Catalytic Activity

After knowing that these non-metal doped CrS₂ candidates exhibit great potential for experimental synthesis, high stability, diverse magnetic moment, and enhanced conductivity, we further explored their catalytic activities towards ORR.

Typically, the O₂ molecule can be reduced to H₂O along a four-electron ($4e^-$) pathway (Figure 3a): (1) $O_2(g) + H^+ + e^- \rightarrow OOH^*$; (2) $OOH^* + H^+ + e^- \rightarrow O^* + H_2O$; (3) $O^* + H^+ + e^- \rightarrow OH^*$; (4) $OH^* + H^+ + e^- \rightarrow H_2O(l)$ [59,60]. We again took the N@CrS₂ monolayer as the representative to compute the ΔG values of the above four elementary steps. As shown in Figure 3b, we found that the formation of OOH* species on the N site of the N@CrS₂ catalyst is exothermic, with a ΔG value of -0.84 eV. The length of the formed N–O bond is 1.41 Å, and the O–O bond is elongated to 1.48 Å as compared with that of the free O₂ molecule (1.23 Å). Subsequently, the approach of a second hydrogen induces the dissociation of OOH* into ($O^* + H_2O$) or the formation of H₂O₂. Remarkably, the OOH* formation is exothermic by 2.43 eV, which is much larger than that of H₂O₂ formation (0.16 eV), suggesting that N@CrS₂ shows a rather high selectivity towards the

$4e^-$ pathway by greatly suppressing the competing $2e^-$ one. Once the O^* species is formed, it can be further hydrogenated to form OH^* and the second H_2O with the ΔG values of -0.83 and -0.82 eV, respectively. According to the CHE model, the final step (i.e., OH^* desorption) is identified as the potential-determining step (PDS). Thus, the limiting potential is 0.82 V, which is the smallest applied voltage to make the whole reaction still exergonic, corresponding to the overpotential of 0.41 V.

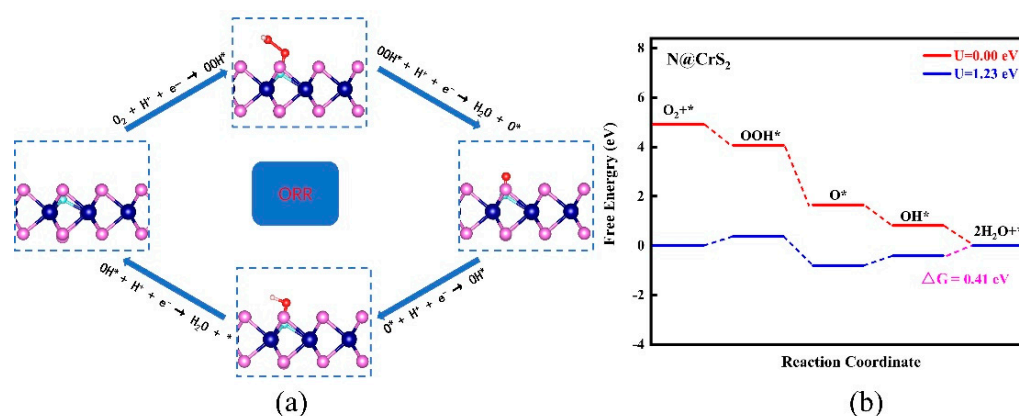


Figure 3. (a) The involved reaction pathway and (b) the computed free energy diagrams for ORR pathways on the $N@CrS_2$ monolayer at zero and applied voltages.

As for other $X@CrS_2$ candidates, the computed free adsorption energies of oxygenated species and the corresponding η^{ORR} are summarized in Table S2. We found that the computed η^{ORR} increases in the order of $As@CrS_2$ (0.97 V) < $C@CrS_2$ (1.20 V) < $O@CrS_2$ (1.53 V) < $Se@CrS_2$ (1.61 V) < $Br@CrS_2$ (1.74 V) \approx $Cl@CrS_2$ (1.78 V) < $P@CrS_2$ (2.18 V) < $B@CrS_2$ (2.42 V) < $Si@CrS_2$ (2.82 V), as shown in Figure S2, which are all higher than that of $N@CrS_2$ (0.41 V). In particular, the overpotential of $N@VS_2$ (0.41 V) is even lower than that of the well-established Pt catalyst (0.45 V) [15], implying its excellent ORR catalytic activity. As ORR usually occurs in aqueous solution, we also studied the solvent effect on the ORR activity of the $N@CrS_2$ catalyst using the implicit solvation model in VASPsol with a dielectric constant of 80 [61]. It can be seen from Figure S3 that the PDS locates at the last step, and the computed η value is 0.48 V, which is comparable to that of the value without the solvent effect (0.41 V), implying that the solvent effects left the superior ORR catalytic performance of the $N@CrS_2$ monolayer nearly unchanged. Although implicit solvent models can offer fast and inexpensive starting points for estimating the solvation effects [62–65], they may not fully describe the interactions of ORR adsorbates with water molecules due to the formation of H-bonds. As an alternative to implicit solvent approaches, explicit solvent models may provide a more comprehensive solution to describe the solvation effects on the ORR catalytic performance, which usually requires sampling thousands of solvent configurations, thus resulting in significant computational expense due to the use of classical molecular dynamic (MD) computations based on force fields. To this end, according to previous studies [66], explicit water layers were employed by placing 10 H_2O molecules on the adsorbed oxygenated species (Figure S4). The results showed that the computed η value for ORR on the $N@CrS_2$ catalyst using the explicit models is 0.50 V (Figure S4), which is close to our implicit solvent value (0.48 V). Thus, the implicit solvation model can also provide a reasonable estimation of the solvation energy for ORR intermediates, consistent with previous theoretical studies [67].

4. Discussion

Based on the well-accepted Sabatier principle, either too strong or too weak adsorption of reaction intermediates on catalysts can result in poor catalytic activity. This is because adsorption that is too strong will hamper the desorption process, resulting in poisoned catalysts, whereas too weak adsorption will induce insufficient activation of intermediates.

Thus, the best catalysts exhibit the optimal adsorption strength with reaction intermediates, which locates at the peak of the volcano plot. Clearly, the ORR's catalytic activity is intrinsically dependent on the adsorption strength of reaction intermediates with catalysts. To this end, we scaled the adsorption free energies of OOH^* (ΔG_{OOH^*}), O^* (ΔG_{O^*}) and OH^* (ΔG_{OH^*}) on different X@CrS_2 systems.

As shown in Figure 4a, obvious linear scaling relationships can be obtained between ΔG_{OOH^*} and ΔG_{OH^*} by $\Delta G_{\text{OOH}^*} = 0.72 \Delta G_{\text{OH}^*} + 3.49$ ($R^2 = 0.97$) as well as ΔG_{O^*} and ΔG_{OH^*} by $\Delta G_{\text{O}^*} = 1.10 \Delta G_{\text{OH}^*} + 0.72$ ($R^2 = 0.89$). Thus, ΔG_{OH^*} can be utilized as an eligible descriptor to describe the catalytic trend of these considered X@CrS_2 catalysts. Furthermore, a volcano plot of ORR activity (η^{ORR}) for X@CrS_2 with the variation in ΔG_{OH^*} is obtained (Figure 4b), in which either a strong Si@CrS_2 or a weak binding strength O@CrS_2 with OH^* species will induce poor ORR activity. On the contrary, the N@CrS_2 catalyst displays a moderate binding strength with OH^* and exhibits high ORR catalytic activity, making it locate at the peak of the volcano curve, and, thus, it becomes the best ORR catalyst among all the studied systems.

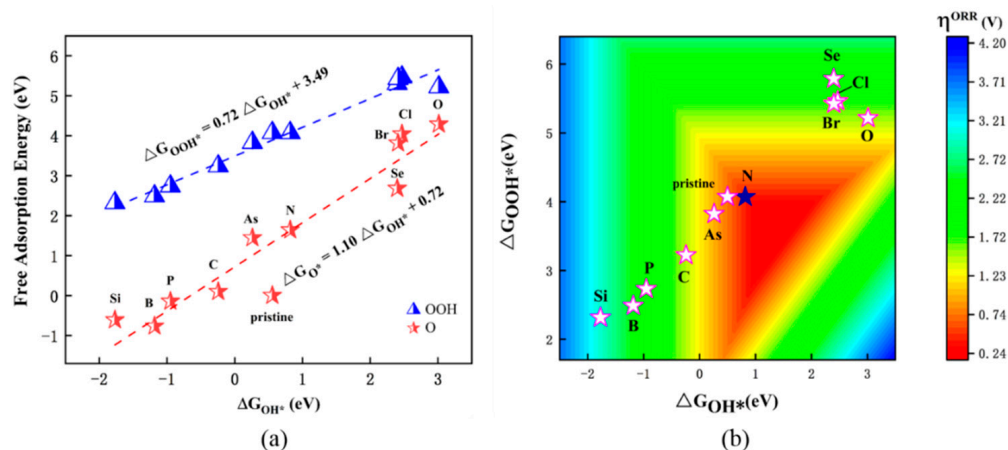


Figure 4. (a) Scaling relations between the free adsorption energies of intermediates (ΔG_{O^*} vs. ΔG_{OH^*} and ΔG_{OOH^*} vs. ΔG_{OH^*}) and (b) η^{ORR} vs. ΔG_{OH^*} on different X@CrS_2 systems.

To gain deep insight into the remarkable difference of OH^* adsorption on X@CrS_2 , we turn to exploring the p-band center (ε_p) model of the non-metal active sites [68], in which Si@CrS_2 , N@CrS_2 , and O@CrS_2 systems were chosen as the representatives of strong, moderate, and weak OH^* adsorption. Notably, according to this model, the position of ε_p closer to the Fermi level will generally induce a stronger interaction of reaction species with catalysts. Our results demonstrated that the computed ε_p values of Si, N, and O dopants are -0.98 , -2.37 , and -3.30 eV, respectively, as shown in Figure 5. The moderate ε_p value on N@CrS_2 suggests its optimal interaction with the oxygenated species, which is responsible for its superior catalytic performance.

In addition, the charge density differences in Si@CrS_2 , N@CrS_2 , and O@CrS_2 with adsorbed OH^* species were computed (Figure 6). Upon OH^* adsorption, we found that the charge depletion around the Si, N, and O endures, while the charge accumulation locates at the X–O bonds, indicating the charge transfer from the catalysts to oxygenated intermediates. According to the Bader charges analysis, the charge transfer is 0.71 , 0.08 , and 0.16 $|e^-|$ for OH^* adsorption on Si@CrS_2 , N@CrS_2 , and O@CrS_2 , respectively, which is consistent with the binding strengths between them. Thus, the moderate adsorption strength of N@CrS_2 endows it with its high ORR catalytic activity.

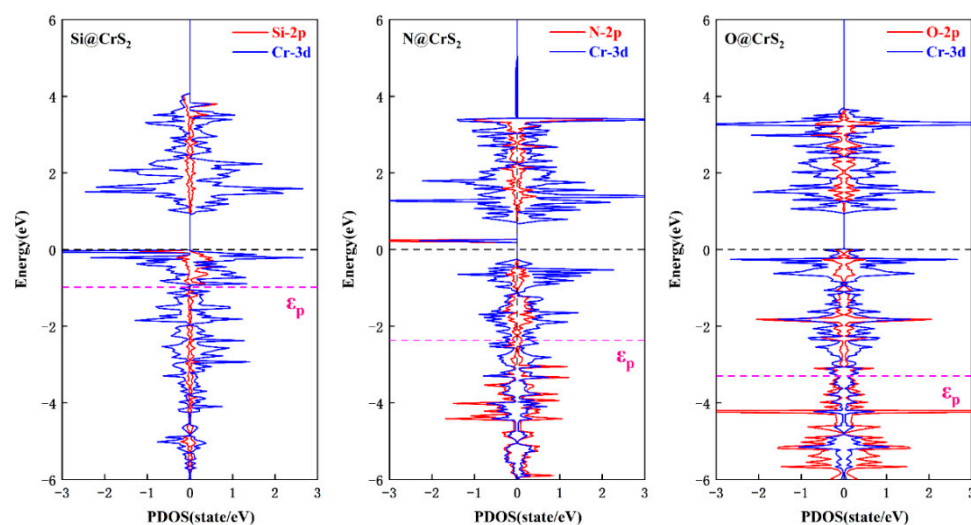


Figure 5. The computed partial density of states for Si@CrS₂, N@CrS₂, and O@CrS₂. The black and pink vertical dotted lines represent the Fermi energy level and p-band center (ϵ_p), respectively.

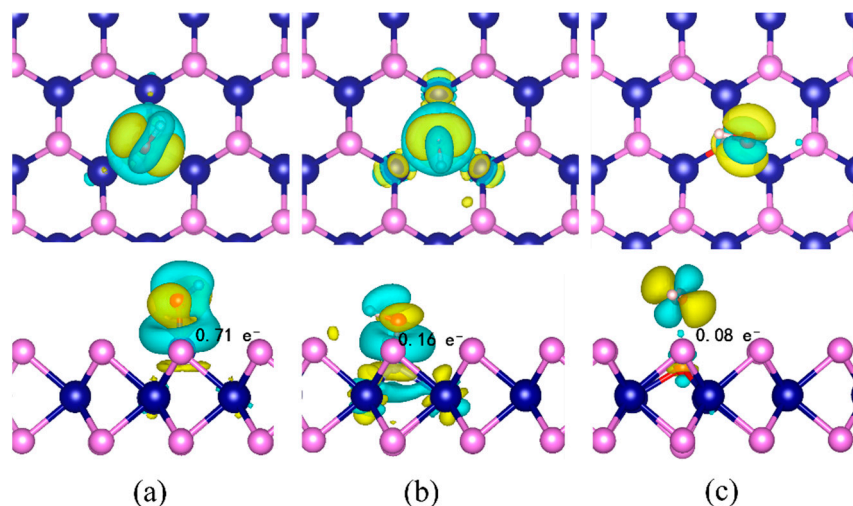


Figure 6. The charge difference density of OH* adsorption on (a) Si@CrS₂N, (b) N@CrS₂, and (c) O@CrS₂ with the isosurface of 0.003 e/Å³. Cyan and yellow bubbles represent positive and negative charges, respectively.

5. Conclusions

In summary, by performing comprehensive DFT computations, we have systematically investigated the structures, stabilities, and magnetic and electronic properties as well as the ORR catalytic activity of several non-metal doped CrS₂ monolayers. Our results demonstrated that most of the doped CrS₂ materials generally possess high stability and hold great promise for experimental synthesis. As expected, depending on the kinds of the incorporated dopants, these CrS₂ monolayers exhibit different magnetic and electronic properties. Based on the computed free energy changes in all elementary steps during ORR, the N@CrS₂ was revealed as a quite promising ORR electrocatalyst due to its lower overpotential (0.41 V) than that of the Pt benchmark (0.45 V). Moreover, obvious scaling linear relationships between oxygenated species can be obtained, which was employed to construct the volcano curve between ORR catalytic activity and OH* binding strength. Understandably, the moderate p-band center and charge transfer from catalyst to oxygenated species render the N@CrS₂ catalyst's optimal interaction with reaction species, thus rationalizing its outstanding ORR catalytic performance. Our findings not only provide a novel

strategy for the design of low-cost, highly-efficient ORR electrocatalysts, but also further widen the potential applications of CrS₂-based materials.

Supplementary Materials: The following supporting information can be downloaded at: <https://www.mdpi.com/article/10.3390/nano12173012/s1>, Figure S1: Total potential temperature and energy fluctuations after equilibration for N@CrS₂ in the AIMD simulation; Figure S2: The computed free energy diagrams for ORR on different X@CrS₂ systems; Figure S3: The computed free energy diagrams for ORR on N@CrS₂ with solvent effect. Figure S4: The computed free energy diagrams and the corresponding intermediates configurations for ORR on N@CrS₂ with the explicit solvent models; Tables S1: The computed the overpotentials (η^{ORR} , V) at various energy cutoff (eV) or k-points; Tables S2: The computed the overpotential (η^{ORR}) and the free adsorption energies (ΔG , eV) for various X@CrS₂ materials.

Author Contributions: Conceptualization, writing—original draft preparation, Z.Q.; validation, Z.W.; writing—review and editing, formal analysis, X.L.; data curation, Q.C.; writing—review and editing, F.L.; Supervision, project administration, J.Z. All authors have read and agreed to the published version of the manuscript.

Funding: This research was funded by Natural Science Funds (NSF) for Distinguished Young Scholar of Heilongjiang Province (No. JC2018004).

Institutional Review Board Statement: Not applicable.

Informed Consent Statement: Not applicable.

Conflicts of Interest: The authors declare no conflict of interest.

References

1. Topsøe, N.-Y. Mechanism of the Selective Catalytic Reduction of Nitric Oxide by Ammonia Elucidated by in Situ On-Line Fourier Transform Infrared Spectroscopy. *Science* **1994**, *265*, 1217–1219. [[CrossRef](#)]
2. Gattuso, J.-P.; Magnan, A.; Billé, R.; Cheung, W.W.L.; Howes, E.L.; Joos, F.; Allemand, D.; Bopp, L.; Cooley, S.R.; Eakin, C.M.; et al. Contrasting futures for ocean and society from different anthropogenic CO₂ emissions scenarios. *Science* **2015**, *349*, aac4722. [[CrossRef](#)]
3. Meng, D.; Zhan, W.; Guo, Y.; Guo, Y.; Wang, L.; Lu, G. A Highly Effective Catalyst of Sm-MnOx for the NH₃-SCR of NO_x at Low Temperature: Promotional Role of Sm and Its Catalytic Performance. *ACS Catal.* **2015**, *5*, 5973–5983. [[CrossRef](#)]
4. Chu, S.; Cui, Y.; Liu, N. The path towards sustainable energy. *Nat. Mater.* **2017**, *16*, 16–22. [[CrossRef](#)]
5. Obama, B. The irreversible momentum of clean energy. *Science* **2017**, *355*, 126–129. [[CrossRef](#)]
6. Wang, L.; Chen, W.; Zhang, D.; Du, Y.; Amal, R.; Qiao, S.; Wu, J.; Yin, Z. Surface strategies for catalytic CO₂ reduction: From two-dimensional materials to nanoclusters to single atoms. *Chem. Soc. Rev.* **2019**, *48*, 5310–5349. [[CrossRef](#)]
7. Dresselhaus, M.S.; Thomas, I.L. Alternative energy technologies. *Nature* **2001**, *414*, 332–337. [[CrossRef](#)]
8. Panwar, N.L.; Kaushik, S.C.; Kothari, S. Role of renewable energy sources in environmental protection: A review. *Renew. Sustain. Energy Rev.* **2011**, *15*, 1513–1524. [[CrossRef](#)]
9. Liu, H.; Logan, B.E. Electricity Generation Using an Air-Cathode Single Chamber Microbial Fuel Cell in the Presence and Absence of a Proton Exchange Membrane. *Environ. Sci. Technol.* **2004**, *38*, 4040–4046. [[CrossRef](#)]
10. Winter, M.; Brodd, R.J. What Are Batteries, Fuel Cells, and Supercapacitors? *Chem. Rev.* **2004**, *104*, 4245–4270. [[CrossRef](#)]
11. Li, Y.; Dai, H. Recent advances in zinc–air batteries. *Chem. Soc. Rev.* **2014**, *43*, 5257–5275. [[CrossRef](#)]
12. Wen, X.; Zhang, Q.; Guan, J. Applications of metal–organic framework-derived materials in fuel cells and metal-air batteries. *Coord. Chem. Rev.* **2020**, *409*, 213214. [[CrossRef](#)]
13. Huang, Z.-F.; Wang, J.; Peng, Y.; Jung, C.-Y.; Fisher, A.; Wang, X. Design of Efficient Bifunctional Oxygen Reduction/Evolution Electrocatalyst: Recent Advances and Perspectives. *Adv. Energy Mater.* **2017**, *7*, 1700544. [[CrossRef](#)]
14. Marković, N.M.; Schmidt, T.J.; Stamenković, V.; Ross, P.N. Oxygen Reduction Reaction on Pt and Pt Bimetallic Surfaces: A Selective Review. *Fuel Cells* **2001**, *1*, 105–116. [[CrossRef](#)]
15. Nørskov, J.K.; Rossmeisl, J.; Logadottir, A.; Lindqvist, L.; Kitchin, J.R.; Bligaard, T.; Jónsson, H. Origin of the Overpotential for Oxygen Reduction at a Fuel-Cell Cathode. *J. Phys. Chem. B* **2004**, *108*, 17886–17892. [[CrossRef](#)]
16. Lim, B.; Jiang, M.; Camargo, P.H.C.; Cho, E.C.; Tao, J.; Lu, X.; Zhu, Y.; Xia, Y. Pd-Pt Bimetallic Nanodendrites with High Activity for Oxygen Reduction. *Science* **2009**, *324*, 1302–1305. [[CrossRef](#)]
17. Nie, Y.; Li, L.; Wei, Z. Recent advancements in Pt and Pt-free catalysts for oxygen reduction reaction. *Chem. Soc. Rev.* **2015**, *44*, 2168–2201. [[CrossRef](#)]
18. Zhang, H.; Liu, L.-M.; Lau, W.-M. Dimension-dependent phase transition and magnetic properties of VS₂. *J. Mater. Chem. A* **2013**, *1*, 10821–10828. [[CrossRef](#)]

19. Lopez-Sanchez, O.; Lembke, D.; Kayci, M.; Radenovic, A.; Kis, A. Ultrasensitive photodetectors based on monolayer MoS₂. *Nat. Nanotechnol.* **2013**, *8*, 497–501. [[CrossRef](#)]
20. Kou, L.; Du, A.; Chen, C.; Frauenheim, T. Strain engineering of selective chemical adsorption on monolayer MoS₂. *Nanoscale* **2014**, *6*, 5156–5161. [[CrossRef](#)]
21. Habib, M.R.; Wang, S.; Wang, W.; Xiao, H.; Obaidulla, S.M.; Gayen, A.; Khan, Y.; Chen, H.; Xu, M. Electronic properties of polymorphic two-dimensional layered chromium disulphide. *Nanoscale* **2019**, *11*, 20123–20132. [[CrossRef](#)]
22. Zhao, R.; Wang, T.; An, Y.; Dai, X.; Xia, C. VS₂ nanosheet as a promising candidate of recycle and reuse NO₂ gas sensor and capturer: A DFT study. *J. Phys. Condens. Matter* **2021**, *33*, 165501. [[CrossRef](#)]
23. Tursun, M.; Wu, C. Electrocatalytic Reduction of N₂ to NH₃ Over Defective 1T'-WX₂ (X=S, Se, Te) Monolayers. *ChemSusChem* **2022**, *15*, e202200191. [[CrossRef](#)]
24. Qin, Z.; Wang, Z.; Zhao, J. Computational screening of single-atom catalysts supported by VS₂ monolayers for electrocatalytic oxygen reduction/evolution reactions. *Nanoscale* **2022**, *14*, 6902–6911. [[CrossRef](#)]
25. Qin, Z.; Zhao, J. 1 T-MoSe₂ monolayer supported single Pd atom as a highly-efficient bifunctional catalyst for ORR/OER. *J. Colloid Interface Sci.* **2022**, *605*, 155–162. [[CrossRef](#)]
26. Ling, F.; Xia, W.; Li, L.; Zhou, X.; Luo, X.; Bu, Q.; Huang, J.; Liu, X.; Kang, W.; Zhou, M. Single Transition Metal Atom Bound to the Unconventional Phase of the MoS₂ Monolayer for Catalytic Oxygen Reduction Reaction: A First-Principles Study. *ACS Appl. Mater. Interfaces* **2021**, *13*, 17412–17419. [[CrossRef](#)]
27. Meza, E.; Diaz, R.E.; Li, C.W. Solution-Phase Activation and Functionalization of Colloidal WS₂ Nanosheets with Ni Single Atoms. *ACS Nano* **2020**, *14*, 2238–2247. [[CrossRef](#)]
28. Zhang, J.; Xu, X.; Yang, L.; Cheng, D.; Cao, D. Single-Atom Ru Doping Induced Phase Transition of MoS₂ and S Vacancy for Hydrogen Evolution Reaction. *Small Methods* **2019**, *3*, 1900653. [[CrossRef](#)]
29. Xiong, Q.; Zhang, X.; Wang, H.; Liu, G.; Wang, G.; Zhang, H.; Zhao, H. One-step synthesis of cobalt-doped MoS₂ nanosheets as bifunctional electrocatalysts for overall water splitting under both acidic and alkaline conditions. *Chem. Commun.* **2018**, *54*, 3859–3862. [[CrossRef](#)]
30. Lv, K.; Suo, W.; Shao, M.; Zhu, Y.; Wang, X.; Feng, J.; Fang, M.; Zhu, Y. Nitrogen doped MoS₂ and nitrogen doped carbon dots composite catalyst for electroreduction CO₂ to CO with high Faradaic efficiency. *Nano Energy* **2019**, *63*, 103834. [[CrossRef](#)]
31. Li, Q.; Guo, Y.; Tian, Y.; Liu, W.; Chu, K. Activating VS₂ basal planes for enhanced NRR electrocatalysis: The synergistic role of S-vacancies and B dopants. *J. Mater. Chem. A* **2020**, *8*, 16195–16202. [[CrossRef](#)]
32. Singh, Y.; Back, S.; Jung, Y. Activating Transition Metal Dichalcogenides by Substitutional Nitrogen-Doping for Potential ORR Electrocatalysts. *ChemElectroChem* **2018**, *5*, 4029–4035. [[CrossRef](#)]
33. Tian, S.; Tang, Q. Activating transition metal dichalcogenide monolayers as efficient electrocatalysts for the oxygen reduction reaction via single atom doping. *J. Mater. Chem. C* **2021**, *9*, 6040–6050. [[CrossRef](#)]
34. Saraf, D.; Chakraborty, S.; Kshirsagar, A.; Ahuja, R. In pursuit of bifunctional catalytic activity in PdS₂ pseudo-monolayer through reaction coordinate mapping. *Nano Energy* **2018**, *49*, 283–289. [[CrossRef](#)]
35. Zhou, W.; Jiang, Z.; Chen, M.; Li, Z.; Luo, X.; Guo, M.; Yang, Y.; Yu, T.; Yuan, C.; Wang, S. Directly anchoring non-noble metal single atoms on 1T-TMDs with tip structure for efficient hydrogen evolution. *Chem. Eng. J.* **2022**, *428*, 131210. [[CrossRef](#)]
36. Chen, K.; Deng, J.; Yan, Y.; Shi, Q.; Chang, T.; Ding, X.; Sun, J.; Yang, S.; Liu, J.Z. Diverse electronic and magnetic properties of CrS₂ enabling strain-controlled 2D lateral heterostructure spintronic devices. *NPJ Comput. Mater.* **2021**, *7*, 79. [[CrossRef](#)]
37. Zhang, J.; Zheng, H.; Han, R.; Du, X.; Yan, Y. Tuning magnetic properties of CrS₂ monolayer by doping transition metal and alkaline-earth atoms. *J. Alloys Compd.* **2015**, *647*, 75–81. [[CrossRef](#)]
38. Kresse, G.; Hafner, J. Ab initio molecular dynamics for liquid metals. *Phys. Rev. B* **1993**, *47*, 558. [[CrossRef](#)] [[PubMed](#)]
39. Kresse, G.; Furthmüller, J. Efficient iterative schemes for ab initio total-energy calculations using a plane-wave basis set. *Phys. Rev. B* **1996**, *54*, 11169. [[CrossRef](#)]
40. Blöchl, P.E. Projector augmented-wave method. *Phys. Rev. B* **1994**, *50*, 17953. [[CrossRef](#)]
41. Kresse, G.; Joubert, D. From ultrasoft pseudopotentials to the projector augmented-wave method. *Phys. Rev. B* **1999**, *59*, 1758. [[CrossRef](#)]
42. Perdew, J.P.; Burke, K.; Ernzerhof, M. Generalized Gradient Approximation Made Simple. *Phys. Rev. Lett.* **1996**, *77*, 3865–3868. [[CrossRef](#)]
43. Tran, F.; Laskowski, R.; Blaha, P.; Schwarz, K. Performance on molecules, surfaces, and solids of the Wu-Cohen GGA exchange-correlation energy functional. *Phys. Rev. B* **2007**, *75*, 115131. [[CrossRef](#)]
44. Ropo, M.; Kokko, K.; Vitos, L. Assessing the Perdew-Burke-Ernzerhof exchange-correlation density functional revised for metallic bulk and surface systems. *Phys. Rev. B* **2008**, *77*, 195445. [[CrossRef](#)]
45. Haas, P.; Tran, F.; Blaha, P. Calculation of the lattice constant of solids with semilocal functionals. *Phys. Rev. B* **2009**, *79*, 085104. [[CrossRef](#)]
46. Haas, P.; Tran, F.; Blaha, P.; Schwarz, K.; Laskowski, R. Insight into the performance of GGA functionals for solid-state calculations. *Phys. Rev. B* **2009**, *80*, 195109. [[CrossRef](#)]
47. Pedroza, L.S.; da Silva, A.J.R.; Capelle, K. Gradient-dependent density functionals of the Perdew-Burke-Ernzerhof type for atoms, molecules, and solids. *Phys. Rev. B* **2009**, *79*, 201106. [[CrossRef](#)]

48. Grimme, S. Semiempirical GGA-type density functional constructed with a long-range dispersion correction. *Phys. Rev. B* **2006**, *27*, 1787. [[CrossRef](#)]
49. Peterson, A.A.; Abild-Pedersen, F.; Studt, F.; Rossmeisl, J.; Nørskov, J.K. How copper catalyzes the electroreduction of carbon dioxide into hydrocarbon fuels. *Energy Environ. Sci.* **2010**, *3*, 1311–1315. [[CrossRef](#)]
50. Tian, X.-H.; Zhang, J.-M. First-Principles Prediction of the Structural, Electronic, and Magnetic Properties of Nonmetal Atoms Doped Single-Layer CrS₂. *Phys. Status Solidi B* **2019**, *256*, 1900149. [[CrossRef](#)]
51. Dolui, K.; Rungger, I.; Das Pemmaraju, C.; Sanvito, S. Possible doping strategies for MoS₂ monolayers: An ab initio study. *Phys. Rev. B* **2013**, *88*, 075420. [[CrossRef](#)]
52. Zhou, J.; Lin, J.; Sims, H.; Jiang, C.; Cong, C.; Brehm, J.A.; Zhang, Z.; Niu, L.; Chen, Y.; Zhou, Y.; et al. Synthesis of Co-Doped MoS₂ Monolayers with Enhanced Valley Splitting. *Adv. Mater.* **2020**, *32*, 1906536. [[CrossRef](#)]
53. Zhang, H.; Tian, Y.; Zhao, J.; Cai, Q.; Chen, Z. Small Dopants Make Big Differences: Enhanced Electrocatalytic Performance of MoS₂ Monolayer for Oxygen Reduction Reaction (ORR) by N- and P-Doping. *Electrochim. Acta* **2017**, *225*, 543–550. [[CrossRef](#)]
54. Li, R.; Yang, L.; Xiong, T.; Wu, Y.; Cao, L.; Yuan, D.; Zhou, W. Nitrogen doped MoS₂ nanosheets synthesized via a low-temperature process as electrocatalysts with enhanced activity for hydrogen evolution reaction. *J. Power Sources* **2017**, *356*, 133–139. [[CrossRef](#)]
55. Xin, X.; Song, Y.; Guo, S.; Zhang, Y.; Wang, B.; Wang, Y.; Li, X. One-step synthesis of P-doped MoS₂ for efficient photocatalytic hydrogen production. *J. Alloys Compd.* **2020**, *829*, 154635. [[CrossRef](#)]
56. Liu, M.; Zhang, R.; Chen, W. Graphene-Supported Nanoelectrocatalysts for Fuel Cells: Synthesis, Properties, and Applications. *Chem. Rev.* **2014**, *114*, 5117–5160. [[CrossRef](#)]
57. Heyd, J.; Scuseria, G.E.; Ernzerhof, M. Hybrid functionals based on a screened Coulomb potential. *J. Chem. Phys.* **2003**, *118*, 8207–8215. [[CrossRef](#)]
58. Wang, Z.; Zhao, J.; Cai, Q.; Li, F. Computational screening for high-activity MoS₂ monolayer-based catalysts for the oxygen reduction reaction via substitutional doping with transition metal. *J. Mater. Chem. A* **2017**, *5*, 9842–9851. [[CrossRef](#)]
59. Li, S.; Miao, P.; Zhang, Y.; Wu, J.; Zhang, B.; Du, Y.; Han, X.; Sun, J.; Xu, P. Recent Advances in Plasmonic Nanostructures for Enhanced Photocatalysis and Electrocatalysis. *Adv. Mater.* **2021**, *33*, 2000086. [[CrossRef](#)]
60. Tong, M.; Sun, F.; Xie, Y.; Wang, Y.; Yang, Y.; Tian, C.; Wang, L.; Fu, H. Operando Cooperated Catalytic Mechanism of Atomically Dispersed Cu–N₄ and Zn–N₄ for Promoting Oxygen Reduction Reaction. *Angew. Chem. Int. Ed.* **2021**, *60*, 14005–14012. [[CrossRef](#)]
61. Mathew, K.; Sundaraman, R.; Letchworth-Weaver, K.; Arias, T.; Hennig, R.G. Implicit solvation model for density-functional study of nanocrystal surfaces and reaction pathways. *J. Chem. Phys.* **2014**, *140*, 084106. [[CrossRef](#)] [[PubMed](#)]
62. Xu, H.; Cheng, D.; Cao, D.; Zeng, X.C. A universal principle for a rational design of single-atom electrocatalysts. *Nat. Catal.* **2018**, *1*, 339–348. [[CrossRef](#)]
63. Chen, Y.; Cheng, T.; Goddard Iii, W.A. Atomistic Explanation of the Dramatically Improved Oxygen Reduction Reaction of Jagged Platinum Nanowires, 50 Times Better than Pt. *J. Am. Chem. Soc.* **2020**, *142*, 8625–8632. [[CrossRef](#)]
64. Mitchell, C.G.; Rachel, M.A.; Derek, J.H.; Yasemin, B.; Donald, F.R.; Steven, A.P.; John, A.K. Doped Amorphous Ti Oxides To Deoptimize Oxygen Reduction Reaction Catalysis. *J. Phys. Chem. C* **2017**, *121*, 16825–16830.
65. Li, F.; Ai, H.; Shen, S.; Geng, J.; Lo, K.H.; Pan, H. Two-Dimensional Dirac Nodal Line Carbon Nitride to Anchor Single-Atom Catalyst for Oxygen Reduction Reaction. *ChemSusChem* **2022**, *15*, e202102537. [[CrossRef](#)]
66. Svane, K.L.; Hansen, H.A.; Vegge, T. A comparison of single and double Co sites incorporated in N-doped graphene for the oxygen reduction reaction. *J. Catal.* **2021**, *393*, 230–237. [[CrossRef](#)]
67. Duan, Z.; Henkelman, G. Identification of Active Sites of Pure and Nitrogen-Doped Carbon Materials for Oxygen Reduction Reaction Using Constant-Potential Calculations. *J. Phys. Chem. C* **2020**, *124*, 12016–12023. [[CrossRef](#)]
68. Zhang, X.; Shi, S.; Gu, T.; Li, L.; Yu, S. The catalytic activity and mechanism of oxygen reduction reaction on P-doped MoS₂. *Phys. Chem. Chem. Phys.* **2018**, *20*, 18184–18191. [[CrossRef](#)]